

NeXtQSM - A complete deep learning pipeline for data-consistent quantitative susceptibility mapping trained with hybrid data *

Francesco Cognolato^{1,2}, Kieran O'Brien^{2,4}, Jin Jin^{2,4}, Simon Robinson^{1,5,6,7}, Frederik B. Laun⁸, Markus Barth^{1,2,3}, and Steffen Bollmann^{1,2,3}

¹ Centre for Advanced Imaging, The University of Queensland, Brisbane, Australia

² ARC Training Centre for Innovation in Biomedical Imaging Technology, The University of Queensland, Brisbane, Australia

³ School of Information Technology and Electrical Engineering, The University of Queensland, Brisbane, Australia

⁴ Siemens Healthcare Pty Ltd, Brisbane, Queensland, Australia

⁵ High Field MR Center, Department of Biomedical Imaging and Image-Guided Therapy, Medical University of Vienna, Vienna, Austria

⁶ Department of Neurology, Medical University of Graz, Graz, Austria

⁷ Karl Landsteiner Institute for Clinical Molecular MR in Musculoskeletal Imaging, Vienna, Austria

⁸ Institute of Radiology, University Hospital Erlangen, Friedrich-Alexander-Universität Erlangen-Nürnberg (FAU), Erlangen, Germany

Abstract. Deep learning based Quantitative Susceptibility Mapping (QSM) has shown great potential in recent years, obtaining similar results to established non-learning approaches. Many current deep learning approaches are not data consistent, require in vivo training data or solve the QSM problem in consecutive steps resulting in the propagation of errors. Here we aim to overcome these limitations and developed a framework to solve the QSM processing steps jointly. We developed a new hybrid training data generation method that enables the end-to-end training for solving background field correction and dipole inversion in a data-consistent fashion using a variational network that combines the QSM model term and a learned regularizer. We demonstrate that NeXtQSM overcomes the limitations of previous deep learning methods. NeXtQSM offers a new deep learning based pipeline for computing quantitative susceptibility maps that integrates each processing step into the training and provides results that are robust and fast.

Keywords: Magnetic Susceptibility · Data-consistent Deep Learning · Electromagnetic Tissue Properties · Simulated Training Data

1 Introduction

Quantitative Susceptibility Mapping (QSM) is a Magnetic Resonance Imaging (MRI) technique which has gained a lot of attention in the last decade because

* The source code will be provided upon request.

of its potential to extract in vivo magnetic susceptibilities [8,41,42]. The quantitative information contained in each voxel linearly reflects the tissue magnetic susceptibility. As a result, QSM is able to reveal information about iron concentrations in the gray matter [1,43,23,40,51,44,20], demyelinating lesions in the white matter [48,50,20], copper accumulation [13], blood oxygenation [10], microbleeds [29] and differentiates them from microcalcifications [39]. Alterations in tissue susceptibility can be linked to ageing [1] as well as neurological diseases such as Parkinson’s disease [2,22], Alzheimer’s disease [3], Huntington’s disease [43] and multiple sclerosis [9,49,54].

The extraction of tissue susceptibilities requires multiple steps in a processing pipeline starting from the phase signal of a gradient-recalled echo (GRE) sequence and includes phase unwrapping, background field removal and dipole inversion (for a review see: [41]). The dipole inversion extracts the susceptibility values and requires the solution of an ill-posed inverse problem. One solution proposed to overcome this ill-posed problem is known as “Calculation of susceptibility through multiple orientation sampling” (COSMOS) [28,47] which requires at least three different orientations to eliminate the singularities in the dipole operation. Despite the high quality of the COSMOS reconstruction, this method is not practical because of its long acquisition time and requiring the measurement of the object in differing rotations.

Due to the impracticability of COSMOS, single orientation solutions have been proposed for phase images. Besides traditional computer vision optimization methods, the recent advent and huge improvements in deep learning techniques [37] led to an application of neural networks to multiple problems in MRI and have shown effectiveness in solving QSM problems such as background field removal [5,27] and dipole inversion [6,52,7,19,14] (for a review see: [16]). However, a limitation of the current state-of-the-art techniques is that the background field correction and dipole inversion are either treated as two independent problems (e.g. [11] does not include background field correction) leading to accumulations of errors between consecutive steps, or do not include a dipole inversion that delivers data consistent solutions (e.g. [45]). Due to the fact that these steps are mostly treated independently, any imprecision or inaccuracies can propagate to the next step affecting the final reconstruction. Total field inversion [17] and Total Generalised Variation (TGV) QSM [21] solve consecutive steps in a single optimization procedure to reduce error propagation. These methods require substantial amounts of compute time due to the difficult optimization problems limiting their application in vivo.

To overcome the computational cost, deep learning methods have been proposed that combine consecutive steps such as the dipole inversion and background field correction [45,26], but these models do not incorporate data-consistency constraints in the dipole inversion. Achieving a data consistent solution would make the reconstruction more robust and invariant to the dipole kernel mag-

netic field direction and has been shown to be a beneficial post-processing step for deep learning solutions [53]. Lastly, most current deep learning QSM techniques require in vivo training data. Often they utilise COSMOS [28] data as a target, which is obtained by multi orientation measurements. Besides the lack of practicality in obtaining such large data sets for training, this is not a realistic target for a single orientation measurement.

To address these limitations, we propose a variational NEural network trained on complex realistic structures for Quantitative Susceptibility Mapping (NeXtQSM). NeXtQSM is an end-to-end deep learning pipeline trained on hybrid data to solve the background field correction and dipole inversion in a data consistent fashion composed by two models which are trained together to solve the two processing steps jointly. Our study is evaluated on data from the QSM reconstruction challenge 2.0 [31] and on in vivo 7T data.

2 Theory

2.1 QSM forward operation

The QSM physical operation is generally described by the equation $Y = \Phi X + \epsilon$, where X is the object in image space containing the susceptibility values, ϵ the noise during the measurement, Y the measured local field and the forward operation $\Phi = F^{-1}DF$ which is a multiplication with the dipole kernel in Fourier domain.

For numerical efficiency, the convolution operation in image space is commonly calculated in Fourier domain F as a pointwise multiplication. The dipole kernel in Fourier space for magnetic fields [38] in the z-axis can be represented with the following equation:

$$D = \frac{1}{3} - \frac{k_z^2}{k_x^2 + k_y^2 + k_z^2} \quad (1)$$

where k_x , k_y and k_z are the k-space values in the respective directions. When the k-space values fraction approaches 1/3, the dipole kernel results to 0, making the dipole inversion ill-posed.

2.2 Variational Networks

These sophisticated models are the bridge connecting iterative methods and deep learning [18]. In iterative methods, the solution of inverse problems can be formulated as an optimization process where at each iteration an objective function $E(x)$ composed by two different terms is minimized:

$$\arg \min_x E = \lambda \underbrace{\|Y - \Phi x\|_2^2}_{f(x)} + \Psi(x) \quad (2)$$

where $f(x)$ is the data consistency term. In this specific case containing the QSM forward model Φ , which helps in applying the model to a variety of

input data that would lead to unstable solutions. $\Psi(x)$ is the regularizer or prior knowledge which prevents overfitting on the data and λ is the learnable trade-off factor between data term and regularizer.

In iterative methods, a hand-crafted prior term Ψ such as Total Variation [34] is chosen. Whereas in variational networks, which can be considered as a hybrid iterative method, the regularizer is learned using convolutional neural networks. At the end of the prefixed number of iterations, a reconstruction error E_{recon} is calculated across the samples in the batch for updating the weights of the neural network:

$$E_{recon} = \sum_{n=0}^N \frac{1}{N} \|\hat{x}_S - X\|_2^2; \quad (3)$$

where \hat{x}_S is the reconstructed susceptibility map and X is the actual ground truth susceptibility values obtained from the hybrid structures.

3 Material and methods

Our pipeline (Fig. 1) learns from realistic simulations of the physical properties of the problem using complex realistic structures which are synthetically created from segmentation maps, see 3.1. The framework is composed of two deep learning architectures trained together in an end-to-end fashion for solving background field removal and dipole inversion. The model solving the background field removal is a standard U-Net [36], whereas the dipole inversion is achieved by a Variational Network [18,19].

3.1 Training data

Due to the lack of ground truth susceptibilities for the dipole inversion and the fact that deep learning techniques need to be trained on fairly large amounts of data to be able to generalize, both of our two models were entirely trained with simulated hybrid data.

The hybrid data are based on the deformation of segmented brain MRI scans using affine transformations and a Gaussian Mixture Model [4], which substituted the class labels with randomly sampled intensities from a prior distribution (Fig. 2). The hybrid data were generated from 28 participants (21 to 34 years of age, average of 26.5 years, 14 males) acquired on a 3 T whole-body MRI scanner (Siemens Healthcare, Erlangen, Germany). The MP2RAGE [30] scans (matrix = 240x256x176, resolution = 1 mm isotropic, GRAPPA = 3, TR = 4000 ms, TE = 2.89 ms, TI1/TI2 = 700/2220 ms) were segmented in 184 classes using FreeSurfer v6 [12]. For each of the 28 healthy individuals, 100 deformed 1 mm isotropic hybrid brains were created with different simulated susceptibility values per region drawing from the initially described normal distribution and used for training our algorithm. We tested larger amounts of training data per

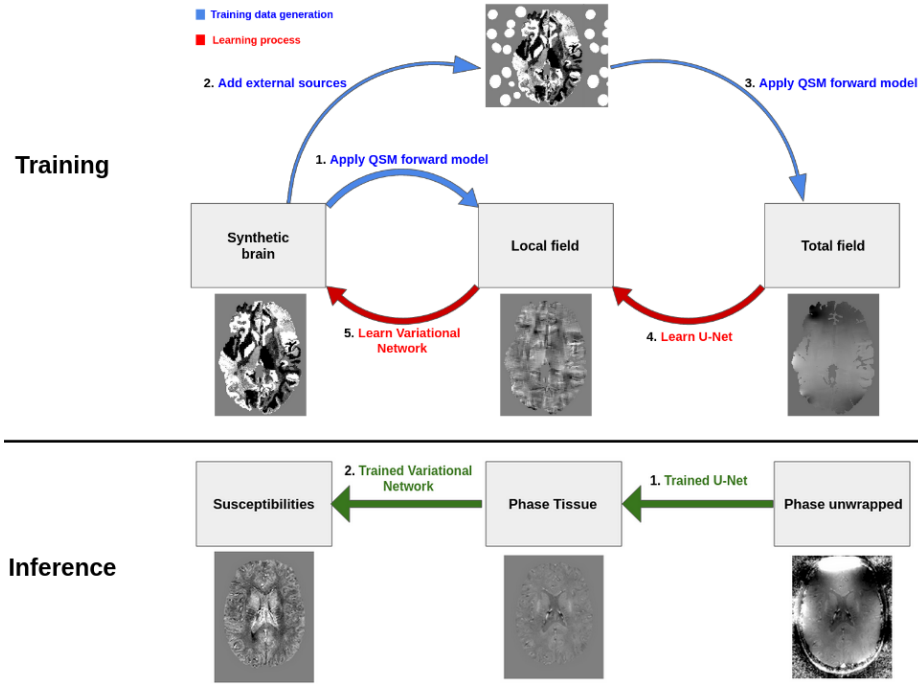


Fig. 1. Illustration of the NeXtQSM pipeline for training (top) and inference time (bottom). The training includes both the training data generation process (blue) and the two deep learning models trained jointly in one optimization (red). In the training data generation (blue), we apply the QSM forward operation to the segmented brains with and without external sources to yield the data for the two learning steps. During training (red), the two architectures are trained in an end-to-end fashion. At inference time (green), the trained models perform the prediction from the unwrapped phase data to the magnetic susceptibility maps.

individual, but did not see any further training improvements. After randomly sampling the intensities per segmentation class, each brain sample was scaled to have 0 mean with a normal distribution whose 1st quartile was set to -0.5 and the 3rd to 0.5.

As shown in the pipeline (Fig. 1), the training data generation was split into two parts: the dipole inversion and the background field removal (local field and total field respectively in Fig. 4). The dipole inversion training data were generated applying the QSM forward operation to the hybrid brains. For the background field removal problem, a random number of around 100 elliptical external sources (Fig. 3), simulating large susceptibility sources such as air (susceptibility value around 9.2 ppm), whose size is randomly sampled around one-tenth of the brain volume. The simulated background field sources were placed randomly around the synthetic brain before convolving it with the QSM forward model

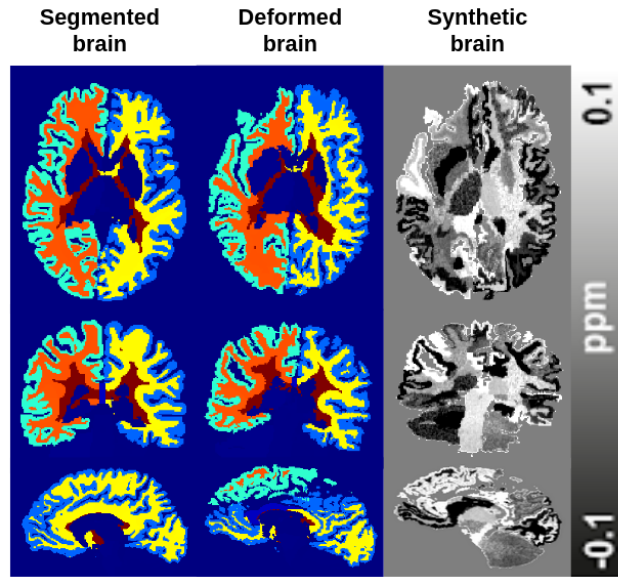


Fig. 2. Visual illustration of the hybrid training data generation. The left column shows the input segmentation map, the center the deformed brain and on the right the results of the random sampling by class using a Gaussian Mixture Model.

(Fig. 1 and 3).

In our previous work (DeepQSM [6]) we showed that the QSM dipole inversion can be solved with neural networks trained purely on simulated data containing simple shapes such as cubes and spheres. However, it was shown later [16] that the simulated data in DeepQSM were not representing brain data well enough and here we improved the training data generation by using more sophisticated and complex brain-like structures that better match the real data distributions in brain scans.

3.2 Testing data

It is common practice in the QSM community to compare the performance of newly developed algorithms to COSMOS [28,47] because of the high fidelity of its reconstruction. However, due to the multiple orientations, it is actually not a good comparison to an algorithm based on a single orientation phase measurement.

Therefore, in order to assess the quality of our reconstruction, we generated a simulated ground-truth QSM dataset using the MATLAB resources provided by the QSM challenge 2.0 [31] organizers which allow to realistically simulate the total field, local field and susceptibility. We were able to generate ground

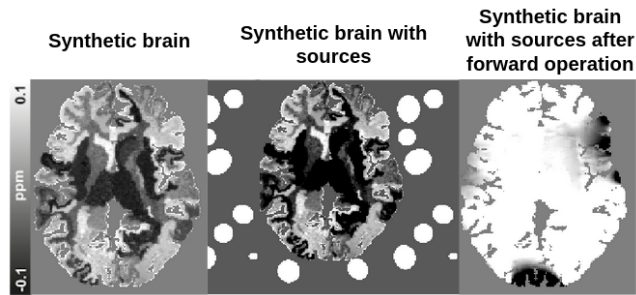


Fig. 3. Illustration of the data generation for the background field removal part. Elliptical sources were randomly placed around the brain, and, after applying the QSM forward model, the background was masked out, leaving only the brain with the effect of the external sources.

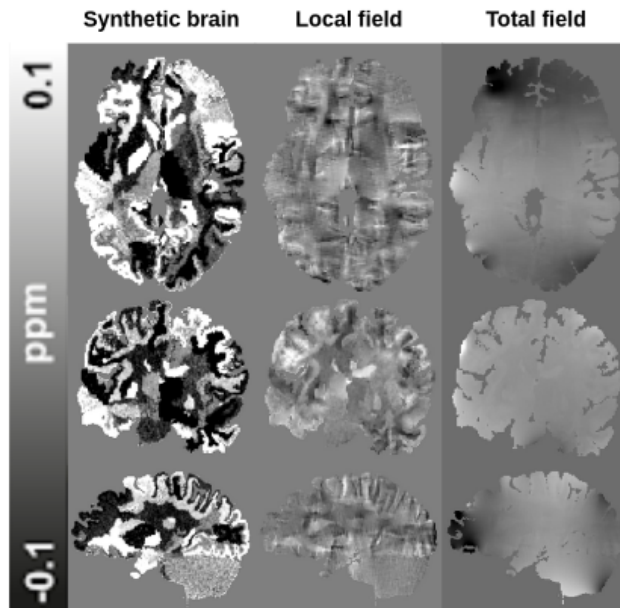


Fig. 4. Illustration of the training dataset. The left column shows the initial hybrid brain with simulated susceptibility values, the center shows the data after application of the QSM dipole model and on the right the data after applying the forward model including the effect of external sources.

truth data for both our background field removal and dipole inversion algorithms using the SIM2 dataset of the challenge. Fig. 5 shows a sample of the simulated testing data. For the QSM challenge testing data, the two parts of the pipeline

have been tested separately using the simulated data as input.

Moreover, we decided to use the same tools from the QSM challenge 2.0 to generate both total and local fields at different resolutions and with different dipole kernel orientations to test the robustness of the algorithm to different input data. In Fig. 11, the inputs at different resolutions and kernel orientations are shown as well as the predictions and corresponding ground truth. We tested our algorithm with data at 0.95 mm and 0.64 mm resolutions using both Z and Y directions of the dipole kernel. Although the training data has a fixed spatial resolution, the dipole kernel in the data term of the variational network is created accordingly to match the input data resolution, allowing the pipeline to be tested at multiple resolutions and kernel orientations.

Besides the data from the QSM challenge 2.0, we tested our pipeline on the second echo of an in vivo 7T scan of a 27 year old male participant. The 7T data were acquired using a multiple echo time gradient-recalled echo (GRE) 3D whole-brain data set: repetition time (TR) = 25 ms, echo time (TE) = 4.4, 7.25, 10.2, 13.25, 16.4, 19.65, 23 ms, flip angle = 13°, field of view (FOV) = $210 \times 181.5 \times 120 \text{ mm}^3$, matrix = $280 \times 242 \times 160$ (0.75 mm isotropic voxels), parallel imaging (generalized autocalibrating partially parallel acquisitions (GRAPPA), acceleration factor = 2, 24 autocalibration lines), monopolar readout gradient, symmetric echo, 1116 Hz/pixel, first echo flow compensated, acquisition time (TA) = 7.9 min. For combining the individual channels we utilized the COMPOSER method [35] with the first echo of a GRE scan (3D GRE with TR = 8 ms, three echoes TE = 1.02, 3.06, 6.12 ms, flip angle = 5°, FOV = $245 \times 245 \times 182 \text{ mm}^3$, matrix = $70 \times 70 \times 52$ (3.5-mm isotropic voxels), monopolar readout gradient, symmetric echo, 1211 Hz/pixel, TA = 24 s). A brain mask was generated using the brain extraction tool BET from FSL [15].

Finally, in order to test the robustness of our pipeline, we apply Gaussian Noise perturbations with 0 mean and 0.005 variance to a control participant dataset acquired at 7T, which is one of our testing datasets used in the results section.

3.3 Pipeline architecture

The first learning block (number 4 in Fig. 1) of the pipeline has the aim to remove background magnetic field contributions from sources which are external to the object during the MR measurement. In particular, this stage uses a U-Net [36] to predict the local field using a feed-forward operation given the total field. The second stage uses a Variational Network [19,18] to enable a data-consistent solution of the QSM dipole inversion. The learned variational network regularizers are implemented using the U-Net architecture [36] at each step. The CNN architecture adjusts its weights during training so that it helps the convergence of the reconstructed volume through a trade-off with the data term.

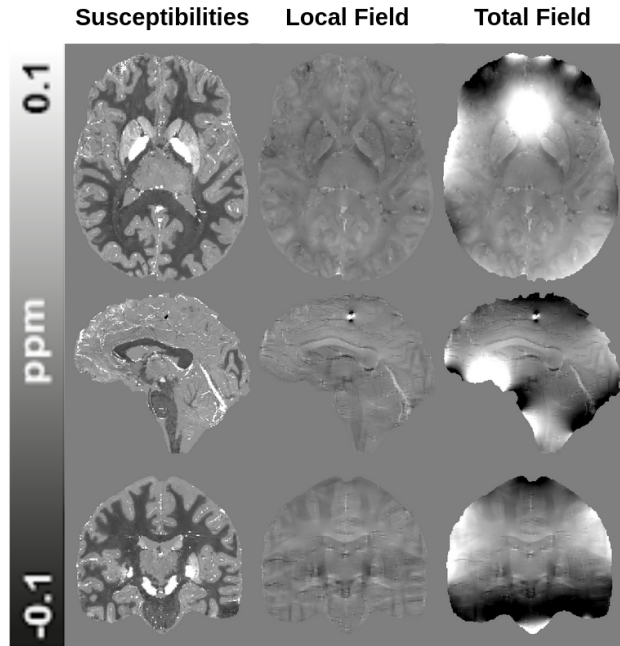


Fig. 5. Sample from the dataset generated from the QSM challenge 2.0 used to test the performance of our algorithm.

3.4 Training procedure

The training was done in an end-to-end fashion, on both the background field and dipole inversion architectures jointly after having trained them separately on our hybrid dataset. At each training epoch, 2'800 hybrid brains were used to learn the problem. The workflow of a training step can be found in Algorithm 1 and is visually illustrated in Fig. 6.

Our end-to-end pipeline was implemented using Tensorflow 2.3.0 and trained for 5 days on a single NVIDIA Tesla V100 32GB GPU with batch size 2. Despite the small batch size, after initial tests we decided to not divide the volumes into smaller 3D patches and fed the complete dataset into the network to better represent the total field to the network architecture.

The end-to-end pipeline was trained for 100 epochs and optimized using Adam optimizer with learning rate $4e-4$ and betas set to 0.9 and 0.999.

3.5 Evaluation

Our end-to-end deep learning pipeline to solve background field removal and dipole inversion was compared both quantitatively on metrics and visually to other methods which offer the solution of these two QSM steps together. Although the pipeline is trained end-to-end, it is possible to visualize intermediate

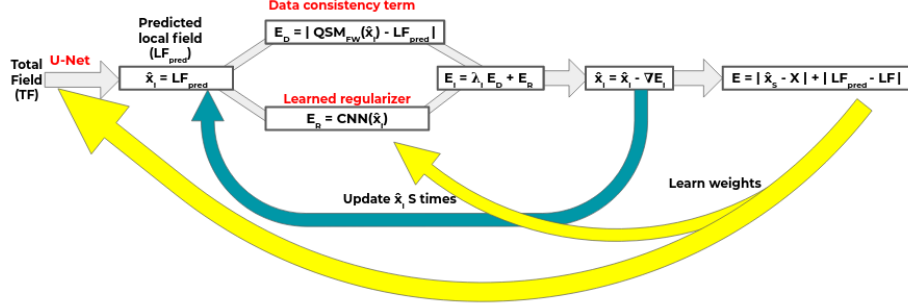


Fig. 6. Graphical description of a training step. The Variational Network loss function is composed of two parts, a data consistency and a regularizer term. X is the hybrid brain, TF total field, LF local field, LF_{pred} the predicted local field, S iterative steps, λ trade-off term, Ψ_i NeuralNet at step i , \hat{x}_S reconstructed volume after S steps. Moreover, the backpropagation procedure is indicated by a yellow arrow which updates the weights of both the U-Net for the background field removal and the regularizer of the variational network.

Algorithm 1: NeXtQSM end-to-end training step. X is hybrid brain, TF total field, LF local field, LF_{pred} the predicted local field, S iterative steps, λ trade-off term, Ψ NeuralNet, N batch size, \hat{x}_S reconstructed volume after S steps. The arrows indicate the assignment to a new variable.

```

 $LF_{pred} \leftarrow UNet(TF)$ 
 $\hat{x}_i \leftarrow LF_{pred}$ 
for  $i < S$  do
   $f(\hat{x}_i) \leftarrow \frac{\lambda_i}{N} \sum_{n=0}^N |LF_{pred} - \Phi \hat{x}_i| + \Psi(\hat{x}_i)$ 
   $\hat{x}_{i+1} \leftarrow \hat{x}_i - \frac{\partial f(\hat{x}_i)}{\partial \hat{x}_i}$ 
end
 $E_{recon} \leftarrow \frac{1}{N} \sum_{n=0}^N |\hat{x}_S - X| + |LF_{pred} - LF|$ 
 $\min E_{recon}$ 

```

results such as the output of the background field removal before being fed into the dipole inversion.

Therefore, we compare background field removal algorithms (LBV [55], V-SHARP [56], Harperella [24] and SHARQnet [5]), dipole inversion algorithms (iLSQR [25], Star-QSM [46], DeepQSM [6], FANSI [32]) as well as algorithms which solve consecutive steps jointly (TGV-QSM [21], AutoQSM [45] and a mix of different background field and dipole inversion algorithms). The final results for FANSI and TGV-QSM have been chosen after fine-tuning the regularization parameters using the L-curve procedure (alpha for FANSI [32] and TGV-QSM [21]).

The results have been compared to other methods using the quantitative metrics NRMSE, HFEN and XSIM [33].

4 Results

4.1 QSM Reconstruction Challenge 2.0

The first experiment to evaluate the performance of the pipeline was performed on data simulated with tools provided by the QSM challenge 2.0 [31].

Fig. 7 shows the result of our background field removal algorithm compared to alternative methods as well as quantitative metrics computed with respect to the simulated ground truth and displayed in Table 1. It can be observed both visually and quantitatively that our background field removal is able to perform on a comparable level to the other considered methods.

Fig. 8 and Table 2 compare our dipole inversion algorithm to other established dipole inversion algorithms. Results of our end-to-end pipeline are compared in the next paragraph with in vivo data of a healthy participant.

Table 1. Quantitative comparison of background field removal methods to simulated local field from QSM challenge 2.0.

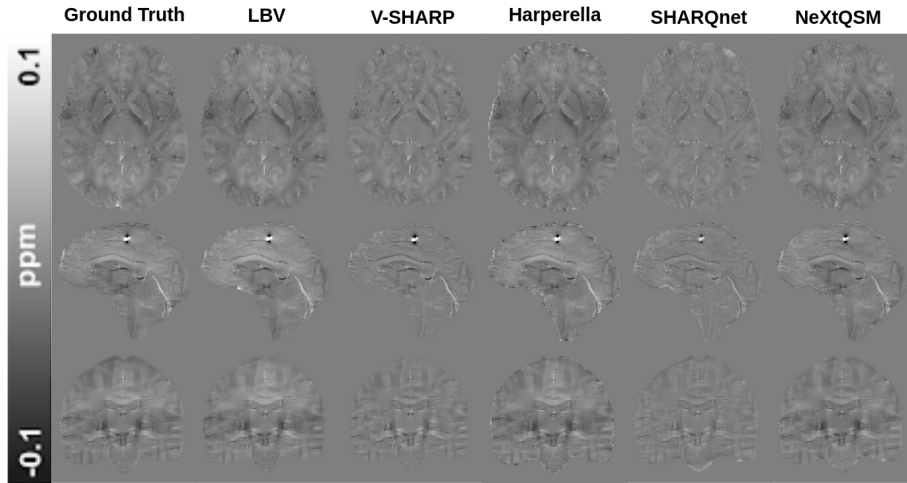
Background Field Removal			
Method	NRMSE	XSIM	HFEN
LBV (MEDI)	51.64	0.86	31.20
V-SHARP	61.58	0.78	37.05
Harperella	60.74	0.83	68.74
SHARQnet	68.93	0.74	45.43
NeXtQSM	50.21	0.83	36.87

4.2 Different resolutions and dipole kernel orientations

The results shown in Fig. 11 demonstrate that NeXtQSM is robust to different resolutions and dipole kernel orientations.

Table 2. Quantitative comparison of dipole inversion reconstruction methods from the simulated local field of the QSM challenge 2.0.

Dipole Inversion			
Method	NRMSE	XSIM	HFEN
iLSQRT	45.31	0.76	49.94
Star-QSM	52.15	0.65	59.22
DeepQSM	84.33	0.30	69.26
FANSI	41.83	0.66	43.06
NeXtQSM	60.81	0.65	60.81

**Fig. 7.** Visual comparison of different methods for removing the background field using the QSM challenge 2.0 data.

4.3 Healthy subject dataset

A second experiment utilized a control participant dataset which is shown in Fig. 12 to show that our end-to-end pipeline is applicable to ultra-high field MRI data. The visual comparison indicates that NeXtQSM delivers a robust background field correction and dipole inversion similar to established QSM methods like TGV-QSM, STI Suite and AutoQSM. It can also be observed that the model agnostic deep learning QSM method SHARQnet + DeepQSM suffers from a lack in contrast and shows residual background field artifacts.

Robustness to Gaussian noise perturbations It can be observed in Fig. 13 that the data consistency constraint in NeXtQSM has a stabilising impact against Gaussian noise perturbation especially in comparison to other deep learning approaches such as SHARQnet + DeepQSM.

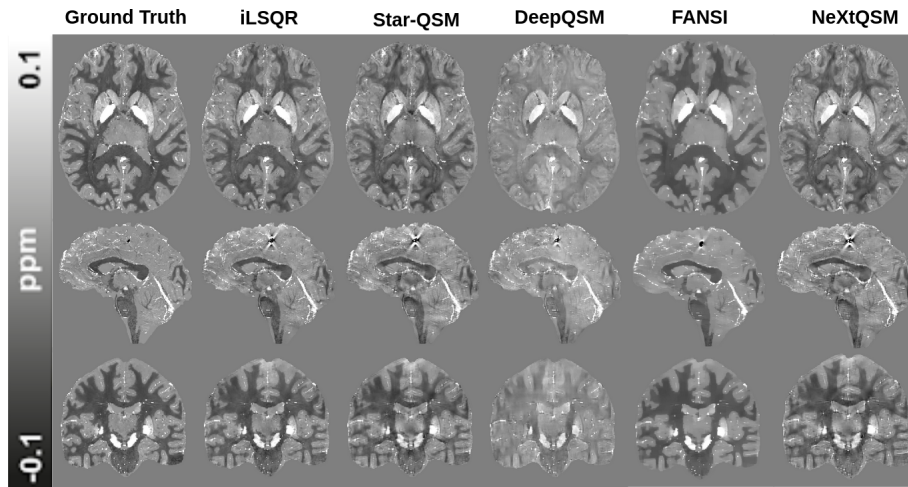


Fig. 8. Visual comparison of different methods for dipole inversion using the QSM challenge 2.0 data.

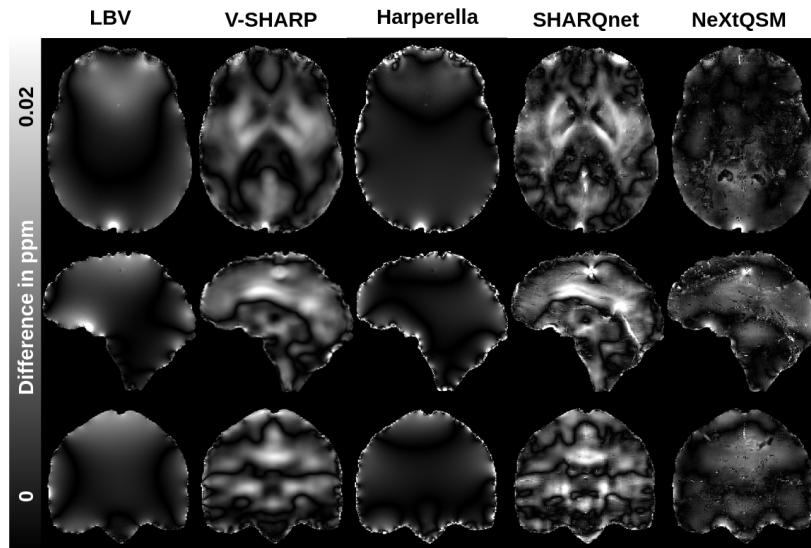


Fig. 9. Difference image of background field removal methods with the simulated ground truth.

We also measured the processing times of the different pipelines (tested on an Intel Core i5-10300H CPU) and the run-times range from 55 s for AutoQSM [45], 500 s for TGV-QSM [21], 160 s for V-Sharp [56] and iLSQR [25], 80 s for

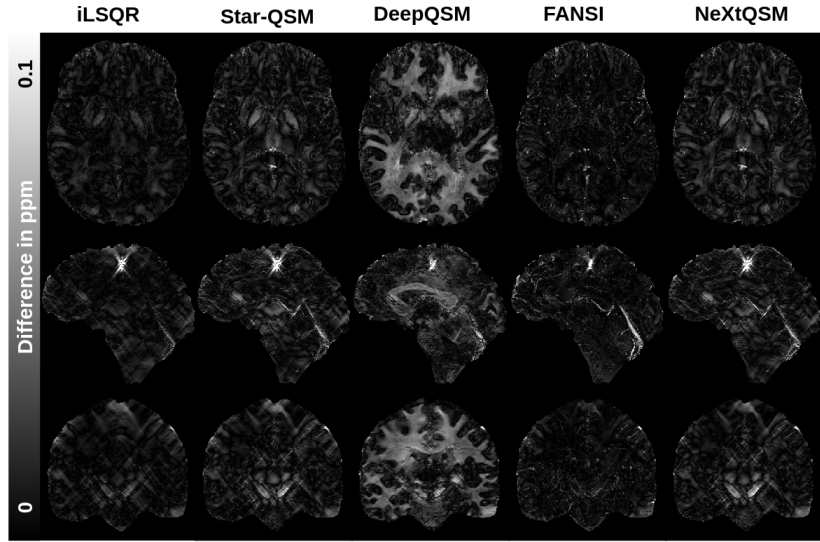


Fig. 10. Difference image of dipole inversion methods with the simulated ground truth.

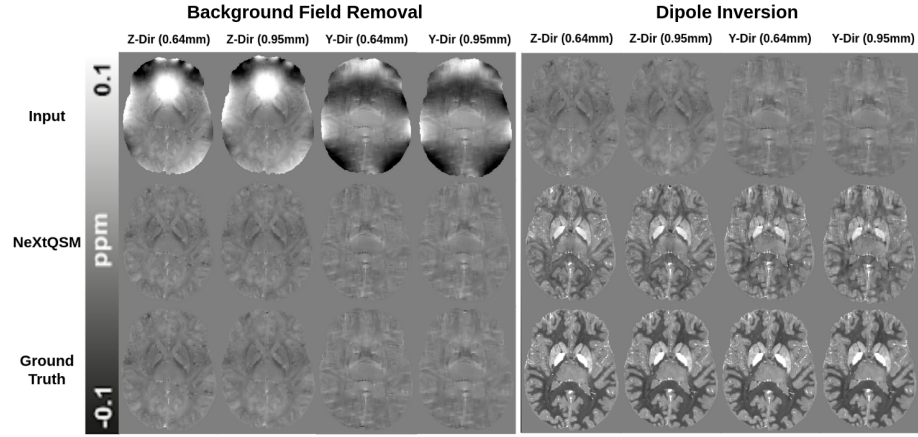


Fig. 11. Visual comparison of NeXtQSM on different resolutions and directions of the dipole kernel. In the first row, the input of the corresponding part is shown, in the second row the output predicted by our model, whereas the last row indicates the ground truth that should have been reconstructed.

Harperella [24] and Star-QSM [46], 70 s for SHARQnet [5] and DeepQSM [6] and 90s for NeXtQSM.

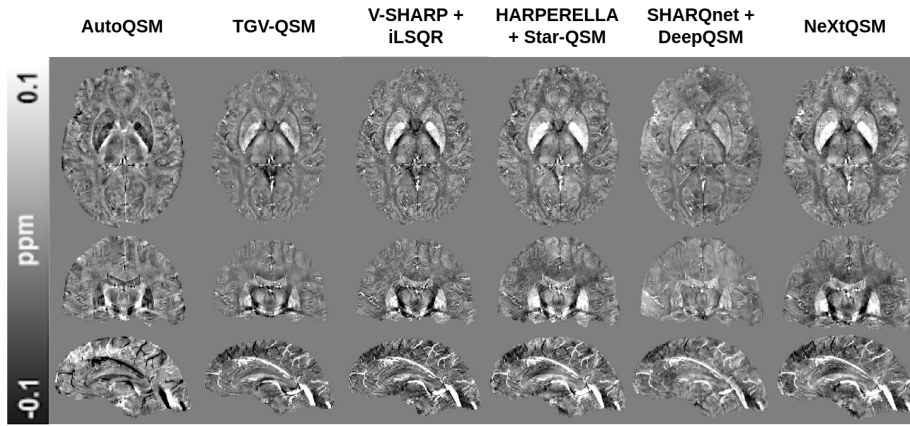


Fig. 12. Visual comparison of different methods using the 7 T control participant dataset. It can be observed that all methods deliver artifact free QSM reconstructions, but SHARQnet and DeepQSM show reduced contrast in comparison to the other methods.

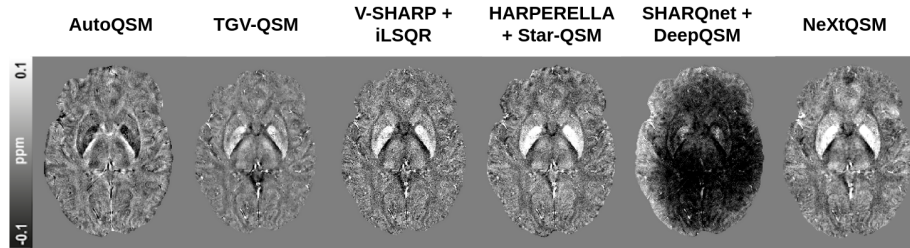


Fig. 13. Visual comparison of the robustness to Gaussian noise perturbations applied to the input. It can be seen that model-agnostic deep learning like SHARQnet and DeepQSM fail to be robust to a change in input data distribution.

5 Discussion

The proposed NeXtQSM pipeline is capable of learning the background field correction and dipole inversion from hybrid training data. We show that the trained networks generalize well to simulated data from the QSM challenge 2.0 and a 7T ultra-high field MRI dataset. When comparing to established QSM algorithms both learning and non-learning based, NeXtQSM’s hybrid training data was shown to capture both the geometrical and physical properties needed to train deep learning models. The data enabled NeXtQSM to learn the QSM dipole model and the effect of external non-brain sources causing the background field. NeXtQSM’s integrated training approach resulted in a pipeline that delivered fast and robust results. Inclusion of the data consistency constraint helped increasing the robustness of the processing to noise and enabled NeXtQSM to

generalize well to in vivo data.

A key difference to existing deep learning QSM solutions is that our framework includes a data consistency constraint for the dipole inversion implemented via a variational network. This increased robustness can be seen for example via a perturbation with Gaussian Noise of the input data resulting in unusable results for a model agnostic deep learning methods, such as DeepQSM and SHARQnet (see Fig. 13). In addition, our pipeline is also robust to a change in resolution and directions of the dipole kernel.

Contrary to earlier work [7,6,5] training NeXtQSM with larger patches was beneficial and did not need to be limited to a training regime that would split-up the brain-volumes in smaller sub-patches. With state-of-the-art GPU hardware we managed to train NeXtQSM with the complete brain volume using a small batch-size. This training regime better matches the theoretical concepts underlying QSM. The background field correction especially profits from a "complete picture" of the artifacts caused by external sources, like air-tissue interfaces.

Although other deep learning approaches have previously attempted to solve the background field removal and dipole inversion in one step [45,26], these methods were very sensitive to slight perturbations in the input data. The training data used were generated from established methods from acquired in vivo datasets which may have biased the learning. The actual physical model utilized to construct our hybrid data means that we could create a large, controllable and independent data set to train on.

Another advantage of NeXtQSM is that it is able to run without any fine-tuning of parameters like in traditional iterative methods. The need of a regularization parameter fine-tuning during inference is a non-negligible limiting factor for QSM clinical applications and clinicians who want a tool which is automated and robust.

Deep learning techniques deliver very fast and high fidelity QSM solutions but the lack of data consistency constraints makes them very sensitive to data distribution changes. Other approaches like TGV-QSM [21] deliver data consistent solutions, but the optimization process is computationally expensive (500s for TGV QSM and 160s for V-Sharp and iLSQR in STI-Suite) limiting their potential clinical applications. NeXtQSM elegantly combines the advantages of deep learning with data consistency concepts used in established QSM inversion techniques to be substantially faster (90 s) than traditional techniques but more robust to input data variations than other deep learning approaches.

Although NeXtQSM delivers quantitative results that are in line with traditional dipole inversion methods, it is not outperforming traditional methods in accuracy or image contrast and we opted for a final result that does not pro-

duce over-regularized maps. Another limitation of NeXtQSM is that it does not suppress the calcification streaking artifact, which is in line with the results of traditional methods like iLSQR and Star-QSM.

6 Conclusion

In this study, we presented NeXtQSM, a deep learning pipeline trained on hybrid samples that integrates and solves QSM’s background field and dipole inversion steps in a data consistent fashion. Our integrated approach is more robust to variations in the input data than other deep learning methods, and substantially faster than iterative QSM techniques.

Acknowledgments

The authors acknowledge the facilities and scientific and technical assistance of the National Imaging Facility, a National Collaborative Research Infrastructure Strategy (NCRIS) capability, at the Centre for Advanced Imaging, the University of Queensland. This research was undertaken with the assistance of resources and services from the Queensland Cyber Infrastructure Foundation (QCIF). Oracle for Research provided Oracle Cloud credits and related resources to support this project. MB acknowledges funding from Australian Research Council Future Fellowship grant FT140100865. SR was supported by the Marie Skłodowska-Curie Action (MS-fMRI-QSM 794298). This research was funded (partially or fully) by the Australian Government through the Australian Research Council (project number IC170100035). Funding for the position of F.B.L. by the German Research Foundation is gratefully acknowledged (LA 2804/12-1).

Conflict of Interest Statement

The presented method has been submitted as a patent application and two co-authors (Kieran O’Brien and Jin Jin) are employees of Siemens Healthcare Pty Ltd.

References

1. Julio Acosta-Cabronero, Matthew J. Betts, Arturo Cardenas-Blanco, Shan Yang, and Peter J. Nestor. In Vivo MRI Mapping of Brain Iron Deposition across the Adult Lifespan. *Journal of Neuroscience*, 36(2):364–374, 2016.
2. Julio Acosta-Cabronero, Arturo Cardenas-Blanco, Matthew Betts, Michaela Butryn, Jose Valdes-Herrera, Imke Galazky, and Peter Nestor. The whole-brain pattern of magnetic susceptibility perturbations in Parkinson’s disease. *Brain : a journal of neurology*, 140, 11 2016.
3. Julio Acosta-Cabronero, Guy B. Williams, Arturo Cardenas-Blanco, Robert J. Arnold, Victoria Lupson, and Peter J. Nestor. In Vivo Quantitative Susceptibility Mapping (QSM) in Alzheimer’s Disease. *PLOS ONE*, 8(11):1–15, 11 2013.

4. Benjamin Billot, Douglas Greve, Koen Van Leemput, Bruce Fischl, Juan Eugenio Iglesias, and Adrian V. Dalca. A Learning Strategy for Contrast-agnostic MRI Segmentation, 2020.
5. Steffen Bollmann, Matilde Holm Kristensen, Morten Skaarup Larsen, Mathias Vassard Olsen, Mads Jozwiak Pedersen, Lasse Riis Østergaard, Kieran O'Brien, Christian Langkammer, Amir Fazlollahi, and Markus Barth. SHARQnet – Sophisticated harmonic artifact reduction in quantitative susceptibility mapping using a deep convolutional neural network. *Zeitschrift für Medizinische Physik*, 29(2):139–149, 2019. Special Issue: Deep Learning in Medical Physics.
6. Steffen Bollmann, Kasper Gade Bøtker Rasmussen, Mads Kristensen, Rasmus Guldhammer Blendal, Lasse Riis Østergaard, Maciej Plochanski, Kieran O'Brien, Christian Langkammer, Andrew L. Janke, and Markus Barth. DeepQSM - Using deep learning to solve the dipole inversion for quantitative susceptibility mapping. *NeuroImage*, 195:373–383, 2019.
7. Yicheng Chen, Angela Jakary, Sivakami Avadiappan, Christopher P. Hess, and Janine M. Lupo. QSMGAN: Improved Quantitative Susceptibility Mapping using 3D Generative Adversarial Networks with Increased Receptive Field, 2019.
8. Andreas Deistung, Ferdinand Schweser, and Jürgen R. Reichenbach. Overview of quantitative susceptibility mapping. *NMR in Biomedicine*, 30(4):e3569, 2017. e3569 NBM-15-0326.R2.
9. Sarah Eskreis-Winkler, Kofi Deh, Ajay Gupta, Tian Liu, Cynthia Wisnieff, Moonsoo Jin, Susan Gauthier, Yi Wang, and Pascal Spincemaille. Multiple sclerosis lesion geometry in Quantitative Susceptibility Mapping (QSM) and phase imaging. *Journal of Magnetic Resonance Imaging*, 42, 08 2014.
10. Audrey Fan, Berkin Bilgic, Louis Gagnon, Thomas Witzel, Himanshu Bhat, Bruce Rosen, and Elfar Adalsteinsson. Quantitative Oxygenation Venography from MRI Phase. *Magnetic resonance in medicine : official journal of the Society of Magnetic Resonance in Medicine / Society of Magnetic Resonance in Medicine*, 72, 07 2014.
11. Ruimin Feng, Jiayi Zhao, He Wang, Baofeng Yang, Jie Feng, Yuting Shi, Ming Zhang, Chunlei Liu, Yuyao Zhang, Jie Zhuang, and Hongjiang Wei. MoDL-QSM: Model-based deep learning for quantitative susceptibility mapping. *NeuroImage*, 240:118376, October 2021.
12. Bruce Fischl, David H. Salat, Evelina Busa, Marilyn Albert, Megan Dieterich, Christian Haselgrove, Andre van der Kouwe, Ron Killiany, David Kennedy, Shuna Klaveness, Albert Montillo, Nikos Makris, Bruce Rosen, and Anders M. Dale. Whole Brain Segmentation: Automated Labeling of Neuroanatomical Structures in the Human Brain. *Neuron*, 33(3):341–355, 2002.
13. Dominik Fritzsche, Martin Reiss-Zimmermann, Robert Trampel, Robert Turner, Karl-Titus Hoffmann, and Andreas Schäfer. Seven-Tesla Magnetic Resonance Imaging in Wilson Disease Using Quantitative Susceptibility Mapping for Measurement of Copper Accumulation. *Investigative radiology*, 49, 11 2013.
14. Yang Gao, Xuanyu Zhu, Bradford A. Moffat, Rebecca Glarin, Alan H. Wilman, G. Bruce Pike, Stuart Crozier, Feng Liu, and Hongfu Sun. xQSM: quantitative susceptibility mapping with octave convolutional and noise-regularized neural networks. *NMR in Biomedicine*, 34(3), Dec 2020.
15. Mark Jenkinson, Christian F. Beckmann, Timothy E.J. Behrens, Mark W. Woolrich, and Stephen M. Smith. Fsl. *NeuroImage*, 62(2):782–790, 2012. 20 YEARS OF fMRI.
16. Woojin Jung, Steffen Bollmann, and Jongho Lee. Overview of quantitative susceptibility mapping using deep learning: Current status, challenges and opportunities. *NMR in Biomedicine*, n/a(n/a):e4292, 2020. e4292 NBM-19-0283.R1.

17. Youngwook Kee, Dong Zhou, Yi Wang, and Pascal Spincemaille. Preconditioned total field inversion (TFI) method for quantitative susceptibility mapping. *Magnetic resonance in medicine*, 78, 07 2016.
18. Erich Kobler, Teresa Klatzer, Kerstin Hammernik, and Thomas Pock. "Variational Networks: Connecting Variational Methods and Deep Learning". In Volker Roth and Thomas Vetter, editors, *Pattern Recognition*, pages 281–293, Cham, 2017. Springer International Publishing.
19. Kuo-Wei Lai, M. Aggarwal, P. V. Zijl, Xuezhe Li, and Jeremias Sulam. Learned proximal networks for quantitative susceptibility mapping. *Medical image computing and computer-assisted intervention : MICCAI International Conference on Medical Image Computing and Computer-Assisted Intervention*, 12262:125–135, 2020.
20. Vera Lambrecht, Jannis Hanspach, Alana Hoffmann, Lisa Seyler, Angelika Mennecke, Sina Straub, Franz Marxreiter, Tobias Bäuerle, Frederik B. Laun, and Jürgen Winkler. Quantitative susceptibility mapping depicts severe myelin deficit and iron deposition in a transgenic model of multiple system atrophy. *Experimental Neurology*, 329:113314, 2020.
21. Christian Langkammer, Kristian Bredies, Benedikt Poser, Markus Barth, Gernot Reishofer, Audrey Fan, Berkin Bilgic, Franz Fazekas, Caterina Mainero, and Stefan Ropele. Fast quantitative susceptibility mapping using 3D EPI and total generalized variation. *NeuroImage*, 111, 02 2015.
22. Christian Langkammer, Lukas Pirpamer, Stephan Seiler, Andreas Deistung, Ferdinand Schweser, Sebastian Frantl, Nina Homayoon, Petra Katschnig-Winter, Mariella Koegl-Wallner, Tamara Pendl, Eva Maria Stoegerer, Karoline Wenzel, Franz Fazekas, Stefan Ropele, Jürgen Rainer Reichenbach, Reinhold Schmidt, and Petra Schwingenschuh. Quantitative Susceptibility Mapping in Parkinson's Disease. *PLOS ONE*, 11(9):1–13, 09 2016.
23. Christian Langkammer, Ferdinand Schweser, Nikolaus Krebs, Andreas Deistung, Walter Goessler, Eva Scheurer, Karsten Sommer, Gernot Reishofer, Kathrin Yen, Franz Fazekas, Stefan Ropele, and Jürgen Reichenbach. Quantitative susceptibility mapping (QSM) as a means to measure brain iron? A post mortem validation study. *NeuroImage*, 62:1593–9, 05 2012.
24. Wei Li, Alexandru V. Avram, Bing Wu, Xue Xiao, and Chunlei Liu. Integrated laplacian-based phase unwrapping and background phase removal for quantitative susceptibility mapping. *NMR in Biomedicine*, 27(2):219–227, 2014.
25. Wei Li, Nian Wang, Fang Yu, Hui Han, Wei Cao, Rebecca Romero, Bundhit Tantiwongkosi, Timothy Q. Duong, and Chunlei Liu. A method for estimating and removing streaking artifacts in quantitative susceptibility mapping. 108:111–122, 2015.
26. Juan Liu and K. Koch. Deep quantitative susceptibility mapping for background field removal and total field inversion. *arXiv: Medical Physics*, 2019.
27. Juan Liu and Kevin M. Koch. "Deep Gated Convolutional Neural Network for QSM Background Field Removal". In Dinggang Shen, Tianming Liu, Terry M. Peters, Lawrence H. Staib, Caroline Essert, Sean Zhou, Pew-Thian Yap, and Ali Khan, editors, *Medical Image Computing and Computer Assisted Intervention – MICCAI 2019*, pages 83–91, Cham, 2019. Springer International Publishing.
28. Tian Liu, Pascal Spincemaille, Ludovic Rochefort, Bryan Kressler, and Yi Wang. Calculation of susceptibility through multiple orientation sampling (COSMOS): A method for conditioning the inverse problem from measured magnetic field map to susceptibility source image in MRI. *Magnetic resonance in medicine : official*

- journal of the Society of Magnetic Resonance in Medicine / Society of Magnetic Resonance in Medicine*, 61:196–204, 01 2009.
29. Tian Liu, Krishna Surapaneni, Min Lou, Liuquan Cheng, Pascal Spincemaille, and Yi Wang. Cerebral Microbleeds: Burden Assessment by Using Quantitative Susceptibility Mapping. *Radiology*, 262:269–78, 11 2011.
 30. José P. Marques, Tobias Kober, Gunnar Krueger, Wietske van der Zwaag, Pierre-François Van de Moortele, and Rolf Gruetter. Mp2rage, a self bias-field corrected sequence for improved segmentation and t1-mapping at high field. *NeuroImage*, 49(2):1271–1281, 2010.
 31. José P. Marques, Jakob Meineke, Carlos Milovic, Berkin Bilgic, Kwok-Shing Chan, Renaud Hedouin, Wietske van der Zwaag, Christian Langkammer, and Ferdinand Schweser. Qsm reconstruction challenge 2.0: A realistic in silico head phantom for mri data simulation and evaluation of susceptibility mapping procedures. *Magnetic Resonance in Medicine*, 86(1):526–542, 2021.
 32. Carlos Milovic, Berkin Bilgic, Bo Zhao, Julio Acosta-Cabronero, and Cristian Tejos. Fast nonlinear susceptibility inversion with variational regularization. *Magnetic Resonance in Medicine*, 80(2):814–821, 2018.
 33. Carlos Milovic, Cristian Tejos, Pablo Irarrazaval, and Karin Shmueli. Xsim, a susceptibility-optimised similarity index metric: Validation with 2016 and 2019 qsm reconstruction challenge datasets, 2022.
 34. Stanley Osher, Wotao Yin, Donald Goldfarb, and Jinjun Xu. An Iterative Regularization Method for Total Variation-Based Image Restoration. *Multiscale Modeling and Simulation Journal*, 4, 01 2005.
 35. Simon Daniel Robinson, Barbara Dymerska, Wolfgang Bogner, Markus Barth, Olga Zanic, Sigrun Goluch, Günther Grabner, Xenia Deligianni, Oliver Bieri, and Siegfried Trattng. Combining phase images from array coils using a short echo time reference scan (composer). *Magnetic Resonance in Medicine*, 77(1):318–327, 2017.
 36. Olaf Ronneberger, Philipp Fischer, and Thomas Brox. U-Net: Convolutional Networks for Biomedical Image Segmentation. *CoRR*, abs/1505.04597, 2015.
 37. Olga Russakovsky, Jia Deng, Hao Su, Jonathan Krause, Sanjeev Satheesh, Sean Ma, Zhiheng Huang, Andrej Karpathy, Aditya Khosla, Michael S. Bernstein, Alexander C. Berg, and Fei-Fei Li. ImageNet Large Scale Visual Recognition Challenge. *CoRR*, abs/1409.0575, 2014.
 38. Rares Salomir, Baudouin Denis de Senneville, and Chrit TW Moonen. A fast calculation method for magnetic field inhomogeneity due to an arbitrary distribution of bulk susceptibility. *Concepts in Magnetic Resonance Part B: Magnetic Resonance Engineering*, 19B(1):26–34, 2003.
 39. Ferdinand Schweser, Andreas Deistung, Berengar W. Lehr, and Jürgen R. Reichenbach. Differentiation between diamagnetic and paramagnetic cerebral lesions based on magnetic susceptibility mapping. *Medical Physics*, 37(10):5165–5178, 2010.
 40. Ferdinand Schweser, Andreas Deistung, Berengar Wendel Lehr, and Jürgen Rainer Reichenbach. Quantitative imaging of intrinsic magnetic tissue properties using MRI signal phase: An approach to in vivo brain iron metabolism? *NeuroImage*, 54(4):2789–2807, 2011.
 41. Ferdinand Schweser, Andreas Deistung, and Jürgen Reichenbach. Foundations of MRI phase imaging and processing for Quantitative Susceptibility Mapping (QSM). *Zeitschrift für medizinische Physik*, 26, 12 2015.
 42. Karin Shmueli, Jacco de Zwart, Peter Gelderen, Tie-Qiang Li, Stephen Dodd, and Jeff Duyn. Magnetic susceptibility mapping of brain tissue in vivo using mri phase

- data. *Magnetic resonance in medicine : official journal of the Society of Magnetic Resonance in Medicine / Society of Magnetic Resonance in Medicine*, 62:1510–22, 12 2009.
43. J.M.G. van Bergen, J. Hua, P.G. Unschuld, I.A.L. Lim, C.K. Jones, R.L. Margolis, C.A. Ross, P.C.M. van Zijl, and X. Li. Quantitative Susceptibility Mapping Suggests Altered Brain Iron in Premanifest Huntington Disease. *American Journal of Neuroradiology*, 37(5):789–796, 2016.
 44. Yi Wang, Pascal Spincemaille, Zhe Liu, Alexey Dimov, Kofi Deh, Jianqi Li, Yan Zhang, Yihao Yao, Kelly Gillen, Alan Wilman, Ajay Gupta, Apostolos Tsiouris, Ilhami Kovanlikaya, Gloria Chiang, Jonathan Weinsaft, Lawrence Tanenbaum, Weiwei Chen, Wenzhen Zhu, Shixin Chang, and Martin Prince. Clinical quantitative susceptibility mapping (QSM): Biometal imaging and its emerging roles in patient care: Clinical QSM Biometals. *Journal of Magnetic Resonance Imaging*, 46, 03 2017.
 45. Hongjiang Wei, Steven Cao, Yuyao Zhang, Xiaojun Guan, Fuhua Yan, Kristen Yeom, and Chunlei Liu. Learning-based single-step quantitative susceptibility mapping reconstruction without brain extraction. *NeuroImage*, 202:116064, 08 2019.
 46. Hongjiang Wei, Russell Dibb, Yan Zhou, Yawen Sun, Jianrong Xu, Nian Wang, and Chunlei Liu. Streaking artifact reduction for quantitative susceptibility mapping of sources with large dynamic range. *NMR in Biomedicine*, 28(10):1294–1303, 2015.
 47. Sam Wharton and Richard Bowtell. Whole-brain susceptibility mapping at high field: A comparison of multiple- and single-orientation methods. *NeuroImage*, 53:515–25, 11 2010.
 48. Samuel Wharton and Richard Bowtell. Effects of white matter microstructure on phase and susceptibility maps. *Magnetic Resonance in Medicine*, 73(3):1258–1269, 2015.
 49. Cynthia Wisnieff, Sriram Ramanan, John Olesik, Susan Gauthier, Yi Wang, and David Pitt. Quantitative susceptibility mapping (QSM) of white matter multiple sclerosis lesions: Interpreting positive susceptibility and the presence of iron. *Magnetic Resonance in Medicine*, 74(2):564–570, 2015.
 50. Zhe Wu, Hongjian He, Yi Sun, Yiping Du, and Jianhui Zhong. High resolution myelin water imaging incorporating local tissue susceptibility analysis. *Magnetic Resonance Imaging*, 42, 06 2017.
 51. Bing Yao, Tie-Qiang Li, Peter Gelderen, Karin Shmueli, Jacco de Zwart, and Jeff Duyn. Susceptibility Contrast in High Field MRI of Human Brain as a Function of Tissue Iron Content. *NeuroImage*, 62:1259–1266, 02 2009.
 52. Jaeyeon Yoon, Enhao Gong, Itthi Chatnuntawech, Berkin Bilgic, Jingu Lee, Woojin Jung, Jingyu Ko, Hosan Jung, Kawin Setsompop, Greg Zaharchuk, Eung Yeop Kim, John Pauly, and Jongho Lee. Quantitative susceptibility mapping using deep neural network: QSMnet. *NeuroImage*, 179:199–206, 2018.
 53. Jinwei Zhang, Zhe Liu, Shun Zhang, Hang Zhang, Pascal Spincemaille, Thanh D. Nguyen, Mert R. Sabuncu, and Yi Wang. Fidelity imposed network edit (FINE) for solving ill-posed image reconstruction. *NeuroImage*, January 2020.
 54. Yan Zhang, Susan Gauthier, Ajay Gupta, Joseph Comunale, Gloria Chiang, Dong Zhou, Weiwei Chen, Ashley Giambone, Wenzhen Zhu, and Yi Wang. Longitudinal change in magnetic susceptibility of new enhanced multiple sclerosis (MS) lesions measured on serial quantitative susceptibility mapping (QSM). *Journal of magnetic resonance imaging : JMRI*, 44, 01 2016.

55. Dong Zhou, Tian Liu, Pascal Spincemaille, and Yi Wang. Background field removal by solving the Laplacian boundary value problem. *NMR in Biomedicine*, 27(3):312–319, 2014.
56. Pinar Senay Özbay, Andreas Deistung, Xiang Feng, Daniel Nanz, Jürgen Rainer Reichenbach, and Ferdinand Schweser. A comprehensive numerical analysis of background phase correction with V-SHARP. *NMR in Biomedicine*, 30(4):e3550, 2017. e3550 NBM-15-0276.R2.